



## RESEARCH ARTICLE

10.1029/2021MS002523

**Special Section:**

Dynamical cores of oceanic models across all scales and their evaluation

# Simulating Linear Kinematic Features in Viscous-Plastic Sea Ice Models on Quadrilateral and Triangular Grids With Different Variable Staggering

C. Mehlmann<sup>1</sup> , S. Danilov<sup>2</sup> , M. Losch<sup>2</sup> , J. F. Lemieux<sup>3</sup> , N. Hutter<sup>2</sup> , T. Richter<sup>4</sup> , P. Blain<sup>5</sup>, E. C. Hunke<sup>6</sup> , and P. Korn<sup>1</sup>

**Key Points:**

- The placement of the sea ice velocity has a mayor influence on the number of simulated linear kinematic features (LKFs)
- The CD-grid resolves twice as many LKFs compared to A, B, C-grids
- A, B, C-grids on quadrilateral meshes resolve a similar number of LKFs as A-grids on triangular meshes (with the same total number of nodes)

**Correspondence to:**

C. Mehlmann,  
[carolin.mehlmann@mpimet.mpg.de](mailto:carolin.mehlmann@mpimet.mpg.de)

**Citation:**

Mehlmann, C., Danilov, S., Losch, M., Lemieux, J. F., Hutter, N., Richter, T., et al. (2021). Simulating linear kinematic features in viscous-plastic sea ice models on quadrilateral and triangular grids with different variable staggering. *Journal of Advances in Modeling Earth Systems*, 13, e2021MS002523. <https://doi.org/10.1029/2021MS002523>

Received 7 MAR 2021  
Accepted 11 OCT 2021

<sup>1</sup>Max-Planck Institute for Meteorology, Hamburg, Germany, <sup>2</sup>Alfred-Wegener-Institut, Helmholtz Zentrum für Polar- und Meeresforschung, Bremerhaven, Germany, <sup>3</sup>Environnement et Changement Climatique Canada, Recherche en Prévision Numérique Environnementale, Dorval, QC, Canada, <sup>4</sup>Otto-von-Guericke Universität Magdeburg, Magdeburg, Germany, <sup>5</sup>Environnement et Changement Climatique Canada, Service Météorologique du Canada, Dorval, QC, Canada, <sup>6</sup>Los Alamos National Laboratory, Los Alamos, NM, USA

**Abstract** Observations in polar regions show that sea ice deformations are often narrow linear features. These long bands of deformations are referred to as Linear Kinematic Features (LKFs). Viscous-plastic sea ice models have the capability to simulate LKFs and more generally sea ice deformations. Moreover, viscous-plastic models simulate a larger number and more refined LKFs as the spatial resolution is increased. Besides grid spacing, other aspects of a numerical implementation, such as the placement of velocities and the associated degrees of freedom, may impact the formation of simulated LKFs. To explore these effects this study compares numerical solutions of sea ice models with different velocity staggering in a benchmark problem. Discretizations based on A-, B-, and C-grid systems on quadrilateral meshes have similar resolution properties as an approximation with an A-grid staggering on triangular grids (with the same total number of vertices). CD-grid approximations with a given grid spacing have properties, specifically the number and length of simulated LKFs, that are qualitatively similar to approximations on conventional Arakawa A-grid, B-grid, and C-grid approaches with half the grid spacing or less, making the CD-discretization more efficient with respect to grid resolution. One reason for this behavior is the fact that the CD-grid approach has a higher number of degrees of freedom to discretize the velocity field. The higher effective resolution of the CD-discretization makes it an attractive alternative to conventional discretizations.

**Plain Language Summary** Sea ice in the Arctic and Antarctic Oceans plays an important role in the exchange of heat and freshwater between the atmosphere and the ocean and hence in the climate in general. Satellite observations of polar regions show that the ice drift sometimes produces long features that are either cracks (leads) and zones of thicker sea ice (pressure ridges). This phenomenon is called deformation. It is mathematically described by the non-uniform way in which the ice moves. For numerical models of sea ice motion it is difficult to represent this deformation accurately. Details of the numerics may affect the way these models simulate leads and ridges, their number and length. Specifically, we find by comparing different numerical models, that the way the model variables are ordered on a computational grid to solve the mathematical equations of sea ice motion has an effect of how many deformation features can be represented on a grid with a given spacing between grid points. A new discretization (ordering of model variables) turns out to resolve more details of the approximated field than traditional methods.

## 1. Introduction

Sea ice is an important component of the climate system. As such, it is crucial for climate models to accurately represent interactions between the atmosphere, the sea ice cover and the ocean. Satellite observations from Synthetic Aperture Radar show that sea ice deformations (i.e., strain rates of the sea ice velocity field) are ubiquitous features of the sea ice cover in polar regions. Sea ice deformations occur over a wide range of spatial scales: from the meter scale to thousands of kilometers (Stern & Lindsay, 2009). Moreover, they are often highly localized and characterized by elongated shapes (Kwok et al., 2008). These elongated bands

© 2021 The Authors. Journal of Advances in Modeling Earth Systems published by Wiley Periodicals LLC on behalf of American Geophysical Union. This is an open access article under the terms of the [Creative Commons Attribution-NonCommercial-NoDerivs License](https://creativecommons.org/licenses/by/4.0/), which permits use and distribution in any medium, provided the original work is properly cited, the use is non-commercial and no modifications or adaptations are made.

of deformations are referred to as Linear Kinematic Features (LKFs). As LKFs are associated with the formation of leads and pressure ridges, they have a strong effect on sea ice production, salt rejection and the associated mixing, as well as on ocean-ice-atmosphere exchanges of momentum, heat and moisture.

For realistic simulations of LKFs, sea ice models require an accurate representation of rheology. Rheology is the relation between applied stresses, mechanical material properties and the resulting deformations. In almost all climate models, sea ice is represented as a continuous viscous-plastic (VP) material (Blockley et al., 2020) either in the classical VP framework (Hibler, 1979) or following the elastic-viscous-plastic (EVP) approximation (Hunke & Dukowicz, 1997), although recently, alternative rheologies have been suggested (Dansereau et al., 2016; Girard et al., 2011; Rampal et al., 2016; Tsamados et al., 2013).

All of these rheologies rely on the continuum assumption, which implies that statistical averages can be taken over a large number of floes or a representative volume element (Feltham, 2008; Gray & Morland, 1994). The validity of the continuum assumption and hence of the VP rheology at grid spacings of the size of ice floes is unclear (Coon et al., 2007; Feltham, 2008). Even so, the majority of practical applications still use the (E)VP model and will do so in the foreseeable future (Blockley et al., 2020).

To some extent, (E)VP models do simulate LKFs (e.g., Hutter & Losch, 2020), reproduce statistics of observed sea ice deformations and spatio-temporal scaling laws (e.g., Bouchat & Tremblay, 2017). As observations, model simulations also display deformations occurring at different spatial scales; a larger number of well defined LKFs are simulated as the grid is refined (e.g., Wang & Wang, 2009).

Various factors affect the number of simulated LKFs, for example, solver convergence (Koldunov et al., 2019; Lemieux et al., 2012), mesh resolution (Hutter et al., 2018; Wang & Wang, 2009), strength parameterization (Hutter & Losch, 2020) and magnitude of the wind stress (Hutchings et al., 2005). These previous studies motivated our interest in further investigating the simulation of LKFs. To our knowledge, this article presents the first study of the impact of the grid staggering of velocity variables on the simulation of LKFs.

To address this question, we define a benchmark problem to compare several spatial discretizations on triangular and quadrilateral meshes with respect to their ability to resolve LKFs. The results are obtained with the *Los Alamos Sea Ice Model* (CICE, Hunke et al., 2015), the sea ice module of the *Massachusetts Institute of Technology general circulation model* (MITgcm, Losch et al., 2010), the *Finite-Volume Sea Ice–Ocean model* (FESOM, Danilov et al., 2015), the sea ice module of the *Icosahedral Nonhydrostatic Weather and Climate Model* (ICON, Mehlmann & Korn, 2021), and also with the academic software library *Gascoigne* (Becker et al., 2021). Note that all different model codes implement the same VP sea ice dynamics. Iterative solutions are either obtained by implicit methods or by modified EVP methods. We indeed show that the staggering of the velocities plays an important role in resolving LKFs, in terms of both total length and number.

The paper is structured as follows. Section 2 presents the viscous-plastic sea ice model. Section 3 describes the benchmark problem. The Arakawa A, B, C, and CD-grid staggering and the corresponding discretization are introduced in Section 4. The numerical results are presented in Section 5 and discussed in Section 6. We conclude in Section 7.

## 2. The Viscous-Plastic Sea Ice Model

For brevity, only a simplified model for three prognostic variables is presented here: the sea ice concentration  $A$ , the mean sea ice thickness  $H$  and the sea ice velocity  $\mathbf{v}$ . The sea ice dynamics are described by a system of coupled partial differential equations:

$$\rho_{ice} H \partial_t \mathbf{v} + f_c e_z \times \mathbf{v} = \text{div } \boldsymbol{\sigma} + A \boldsymbol{\tau}(\mathbf{v}) - \rho_{ice} H g \nabla \tilde{H}_g, \quad (1)$$

$$\partial_t A + \text{div}(\mathbf{v}A) = 0, \quad A \leq 1, \quad (2)$$

$$\partial_t H + \text{div}(\mathbf{v}H) = 0, \quad (3)$$

where  $\rho_{ice}$  is the ice density,  $f_c$  is the Coriolis parameter,  $g$  is the gravitational acceleration,  $\tilde{H}_g$  is the sea surface height and  $e_z$  is the vertical ( $z$ -direction) unit vector. In this form, Equations 2 and 3 neglect all thermodynamic source terms. The forcing term  $\boldsymbol{\tau}(\mathbf{v})$  is the sum of the ocean and atmospheric surface stresses

$$\boldsymbol{\tau}(\mathbf{v}) = C_w \rho_w \|\mathbf{v}_w - \mathbf{v}\|_2 (\mathbf{v}_w - \mathbf{v}) + C_a \rho_a \|\mathbf{v}_a\|_2 \mathbf{v}_a, \quad (4)$$

where  $\mathbf{v}_w$  and  $\mathbf{v}_a$  are the surface ocean velocity and surface wind vectors.

**Table 1**  
Physical Parameters of the Momentum Equation

Parameter	Definition	Value
$\rho_{ice}$	Sea ice density	900 kg/m <sup>3</sup>
$\rho_a$	Air density	1.3 kg/m <sup>3</sup>
$\rho_w$	Water density	1,026 kg/m <sup>3</sup>
$C_a$	Air drag coefficient	$1.2 \cdot 10^{-3}$
$C_w$	Water drag coefficient	$5.5 \cdot 10^{-3}$
$f_c$	Coriolis parameter	$1.46 \cdot 10^{-4} s^{-1}$
$P^*$	Ice strength parameter	$27.5 \cdot 10^3 N/m^2$
$C$	Ice concentration parameter	20
$e$	Ellipse aspect ratio	2

The internal stresses in the ice  $\sigma$  are modeled by the viscous-plastic (VP) sea ice rheology (Hibler, 1979).

The nonlinear viscous-plastic rheology relates the strain rate tensor

$$\dot{\epsilon} = \frac{1}{2} (\nabla \mathbf{v} + \nabla \mathbf{v}^T), \quad \dot{\epsilon}' := \dot{\epsilon} - \frac{1}{2} \text{tr}(\dot{\epsilon}) I, \quad (5)$$

where  $\text{tr}(\cdot)$  is the trace, to the stress tensor  $\sigma$ . The relationship is given by

$$\sigma = 2\eta \dot{\epsilon}' + \zeta \text{tr}(\dot{\epsilon}) I - \frac{P}{2} I, \quad (6)$$

with the viscosities  $\eta$  and  $\zeta$ , given by  $\eta = e^{-2\zeta}$  and

$$\zeta = \frac{P_0}{2\Delta(\dot{\epsilon})}, \quad \Delta(\dot{\epsilon}) := \sqrt{\frac{2}{e^2} \dot{\epsilon}' : \dot{\epsilon}' + \text{tr}(\dot{\epsilon})^2 + \Delta_{\min}^2}. \quad (7)$$

$\Delta_{\min} = 2 \cdot 10^{-9} s^{-1}$  is the threshold that describes the transition between the viscous and the plastic regimes. The replacement pressure  $P$  and the ice strength  $P_0$  in Equation 6 are respectively expressed as

$$P = P_0 \frac{\Delta}{(\Delta + \Delta_{\min})}, \quad P_0(H, A) = P^* H \exp(-C(1 - A)). \quad (8)$$

All parameters values are summarized in Table 1.

The standard approach for solving the coupled sea ice system (Equations 1–3) is a time splitting method (Lemieux et al., 2014). We first compute the solution of the sea ice momentum Equation 1, followed by the solution of the transport Equations 2 and 3. For stability reasons, a fully explicit time stepping scheme for the momentum equation with a VP rheology requires a time step smaller than a second even on a grid resolution as coarse as 100 km (Ip et al., 1991), so that implicit methods in time are necessary. An implicit time discretization requires iterative methods such as a Picard solver (Lemieux & Tremblay, 2009; Zhang & Hibler, 1991) or Newton methods (Lemieux et al., 2010; Losch et al., 2014; Mehlmann & Richter, 2017b). To avoid an implicit discretization, the EVP model was introduced (Hunke & Dukowicz, 1997) where an artificial elastic term added to the VP rheology allows an explicit discretization of the momentum equation with relatively large time steps. However, the original EVP model does not lead to the same deformations as simulated with a VP model. Thus, a modified version of the EVP method was developed that ensures convergence to the solution of the VP model (Bouillon et al., 2013; Kimmritz et al., 2015; Lemieux et al., 2012). We refer to this pseudo-time stepping method as the mEVP solver. In this manuscript, we use an implicit time discretization and solver of the VP model, when available (CICE, Gascoigne, MITgcm), and otherwise the mEVP method (FESOM, ICON). We discuss this choice in Section 6.

## 2.1. Method Section

We evaluate the shear deformation  $\epsilon_{II}$  to quantify the effect of velocity staggering on the formation of LKFs:

$$\epsilon_{II} = \sqrt{(\dot{\epsilon}_{11} - \dot{\epsilon}_{22})^2 - 4\dot{\epsilon}_{12}^2}, \quad (9)$$

where  $\dot{\epsilon}_{11}$ ,  $\dot{\epsilon}_{22}$  and  $\dot{\epsilon}_{12}$  are the elements of the strain rate tensor given in Equation 5. LKFs are detected following Hutter et al. (2019) and the number of LKFs and the total length of all LKFs combined are used as metrics for comparing simulation. The combination of the two metrics adds some robustness to the analysis because the detection algorithm sometimes splits features at intersections leading to an overestimate of the number of LKFs. As the detection algorithm requires gridded data, all model fields are interpolated on a 2 km regular Cartesian mesh. We adapt the original algorithm (Hutter et al., 2019) for our idealized experiments by the following minor changes: (a) We do not use the histogram equalization in the LKF pixel filtering process, as all simulated shear fields have the same range of magnitudes. (b) The maximum and minimum kernel sizes of the Difference of Gaussian (DoG) filter is set to  $6 \cdot \frac{\Delta x}{2 \text{ km}}$  and  $1.2 \cdot \frac{\Delta x}{2 \text{ km}}$ , to ensure that the detected LKFs are wider than one pixel and no grid-scale noise is detected. Here,  $\Delta x$  is the length of the grid edge. (c) We use a filter threshold 0.1 for the DoG using the logarithmic representation of the shear deformation. (d) LKFs with a length below  $4.8 \cdot \Delta x$  are discarded to make sure that the detected LKFs have an aspect ratio of at least 4.

## 2.2. Data and Software Availability Statement

Data sets for this research as well as routines to process it are available in (Mehlmann et al., 2021) and freely and anonymously accessible via <https://data.mendeley.com/datasets/kj58y3sdtk/1>.

## 3. Benchmark Problem

The benchmark problem describes the deformation of sea ice caused by a moving cyclone. We consider the quadratic domain  $\Omega = (0, 512 \text{ km})^2$  with the spatial points  $(x, y) \in \Omega$  given in kilometers. The simulation is run for  $T = [0, 2]$  days, where the time  $t$  is measured in days. Inspired by Hunke (2001) we prescribe a circular steady ocean current

$$\mathbf{v}_w = v_w^{\max} \begin{pmatrix} (2y - L)/L \\ -(2x - L)/L \end{pmatrix}, \quad (10)$$

with  $L = 512 \text{ km}$  and

$$v_w^{\max} = 0.01 \text{ m s}^{-1}.$$

The wind field is described by an anti-cyclone which moves from the center of the domain to the upper right corner. The center of the anti-cyclone moves in time as

$$m_x(t) = m_y(t) = 256 \text{ km} + 51.2 \text{ km day}^{-1} \cdot (t). \quad (11)$$

The maximal wind speed is set to  $v_a^{\max} = \frac{30}{e} \text{ m s}^{-1} \approx 11 \text{ m s}^{-1}$ . To reduce the wind speed away from the center, it is multiplied by the factor

$$s = \frac{e}{100} \exp\left(-\frac{r}{100 \text{ km}}\right), \quad r = \sqrt{(m_x - x)^2 + (m_y - y)^2}. \quad (12)$$

The anti-cyclonic surface wind velocity is expressed as

$$\mathbf{v}_a = -s \cdot v_a^{\max} \begin{pmatrix} \cos(\alpha)(x - m_x) + \sin(\alpha)(y - m_y) \\ -\sin(\alpha)(x - m_x) + \cos(\alpha)(y - m_y) \end{pmatrix}, \quad (13)$$

where we selected  $\alpha = 72^\circ$ .  $90 - \alpha = 18^\circ$  describes the (arbitrarily chosen) deviation of the wind vector from geostrophy. The wind and ocean current are visualized in Figure 1.

We initialize the simulation with sea ice at rest and assume a constant ice concentration of 1.0 and a small perturbation of the ice thickness around a mean of  $H^0(x, y) = 0.3 \text{ m}$ . These initial conditions are

$$\mathbf{v}(0, x, y) = \mathbf{v}^0(x, y) = \mathbf{0} \text{ m s}^{-1}, \quad (14)$$

$$A(0, x, y) = A^0 = 1, \quad (15)$$

$$H(0, x, y) = H^0(x, y) = 0.3 \text{ m} + 0.005 \text{ m} \left( \sin\left(\frac{60x}{1000 \text{ km}}\right) + \sin\left(\frac{30y}{1000 \text{ km}}\right) \right), \quad (16)$$

where  $x, y$  are given in km. At the boundary of the domain we apply a no-slip condition for the velocity:

$$\mathbf{v} = \mathbf{0} \text{ on } \partial\Omega. \quad (17)$$

The benchmark problem is designed so that both the gradient of anti-cyclonic wind field (Equation 13) and boundary condition (Equation 17) lead to LKFs.

## 4. Discretization

Most sea ice models use structured (quadrilateral) meshes and either an Arakawa B-grid like in CICE (Hunke et al., 2015) or Arakawa C-grid discretization as in the sea ice module of the MITgcm (Losch et al., 2010). We are not aware of any sea ice models on Arakawa A-grids or CD-grids on quadrilateral meshes. Some recent sea ice model developments use unstructured meshes with triangular elements. This includes the

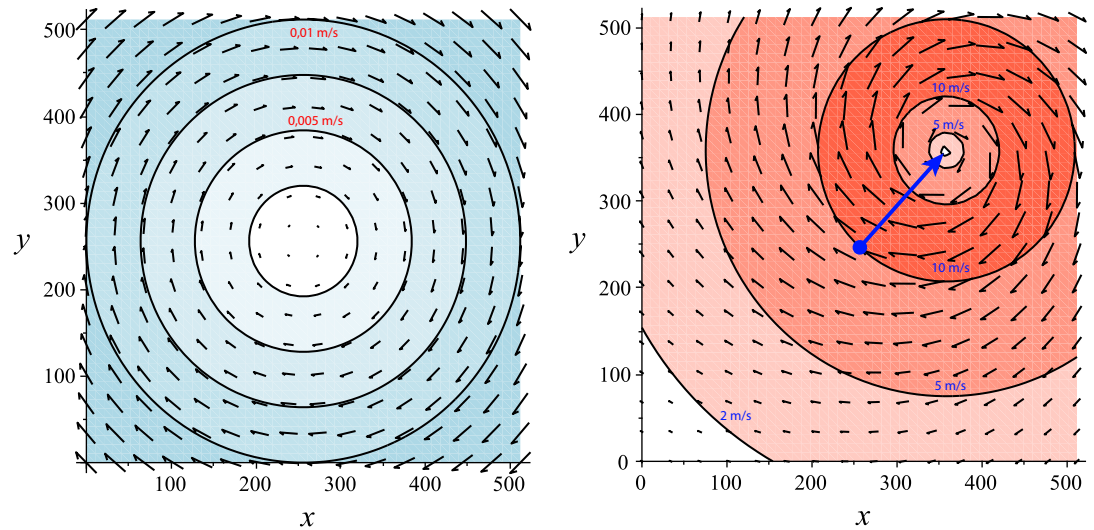


**Figure 1.** Stationary velocity field of the ocean current (left hand side) and wind field at time  $t = 2$  days (right hand side). The bold blue arrow indicates the displacement of the atmospheric anti-cyclone from day zero to day two.

A-grid-like discretization in the sea ice component of FESOM (Danilov et al., 2015), the CD-grid-like discretization in the sea ice module of ICON (Mehlmann & Korn, 2021) and a quasi-B grid discretization in the sea ice module of the *Finite-Volume Community Ocean Model* (FVCOM, Gao et al., 2011). The latter is similar to the quasi-B grid staggering realized on hexagonal meshes in the *Model for Prediction Across Scales* (MPAS, Petersen et al., 2019). In this paper, we compare discretization of the viscous-plastic sea ice model with an Arakawa A-grid, B-grid, C-grid and CD-grid staggering of velocities on structured quadrilateral grids (upper row in Figure 2) and triangular meshes (lower row in Figure 2).

We note that different approaches vary in the number of degrees of freedom of the velocity field (DoFs), which are defined per unknown, by the numbers of vertices, cells and edges. On quadrilateral meshes the CD-grid has  $2N$  DoFs (with  $N$  the number of grid vertices), whereas A, B, C-grid contains  $N$  DoFs. On triangular grids, the A-grid-like approximation has  $N$  DoFs. This is increased by factor 1.5 in case of the B-grid staggering and tripled in the CD-grid discretization. To illustrate this, the degrees of freedom for the grid with 2 km mesh spacing are given in Table 2.

#### 4.1. Model Configuration

In the following we describe the discretization of the benchmark problem (Section 3) in the different models. An overview is provided in Table 2.

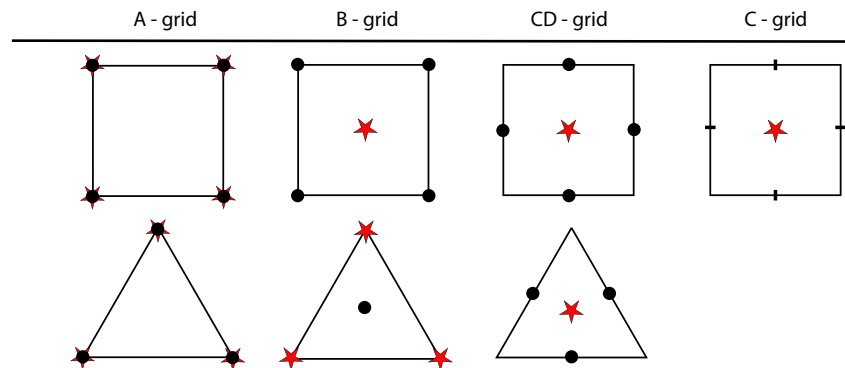


**Figure 2.** Different staggering explored in this manuscript. We indicate the placement of the latitude/zonal velocity  $v = (u, v)$ , the normal component of the velocity and the tracers by  $\bullet$ ,  $*$ , and  $\star$ , respectively.

**Table 2**  
*Overview of the Model Configuration*

Model	Grid	Staggering	Solver	Transport	DoF (2 km)
Gascoigne	□	A	Newton	FEM-FCT	130,560
	□	B	Newton	Upwind	130,560
	□	CD	Newton	Upwind	261,120
MITgcm	□	C	Newton	FV with flux limiter	130,560
CICE	□	B	Picard	Remapping	130,560
FESOM	△	A	mEVP	FEM-FCT	132480 <sup>1</sup> /152736 <sup>2</sup>
	△	B	mEVP	FEM-FCT	303260 <sup>2</sup>
	△	CD	mEVP	Upwind	395378 <sup>1</sup> /455994 <sup>2</sup>
ICON	△	CD	mEVP	Upwind	4487186 <sup>2</sup>

*Note.* The superscript 1 marks the degrees of freedom (DoF) on the triangular grid with the same total number of vertices as the quadrilateral mesh, whereas the 2 indicates the DoF of the mesh which consists triangles with a side length of 2 km.

#### 4.1.1. Gascoigne (A-Grid, B-Grid and CD-Grid Staggering on Quadrilaterals)

We implemented the benchmark problem in the academic software library Gascoigne 3D (Becker et al., 2021). Gascoigne is a flexible toolkit that provides basic routines to discretize two or three dimensional partial differential equations with finite elements. Further, Gascoigne provides high level routines for working with adaptive meshes as well as efficient linear and nonlinear solvers based on Newton-Krylov multigrid methods. For an overview we refer to Richter (2017).

In the framework of Gascoigne we compare finite element discretizations that are based on an A-grid, B-grid or CD-grid placement of the variables. The finite element with a C-grid staggering is not considered as the corresponding finite element space is not large enough to approximate the full strain rate tensor (Acosta et al., 2011) of the VP sea ice rheology. The Arakawa A-grid, B-grid, and CD-grid staggering corresponds to the Q1-Q1, Q1-Q0, and CR-Q0 finite element pairs. The first component of the pair refers to the discretization of the sea ice velocity, and the second component addresses the discretization of the sea ice thickness and concentration. Q0 denotes the piecewise constant element and Q1 refers to the bilinear quadrilateral element (Braess, 2007). On quadrilaterals, CR is the nonconforming rotated bilinear element (Rannacher & Turek, 1992), which is a variant of the triangular nonconforming piecewise linear Crouzeix-Raviart element (Crouzeix & Raviart, 1973). Discretizing the sea ice momentum equation on quadrilateral and triangular meshes with the CD-grid-like CR-element causes oscillations in the velocity field. This instability has its origin in the discretization of the strain rate tensor, which is part of the viscous-plastic rheology (Mehlmann & Korn, 2021). To reduce these oscillations, an edge based stabilization is used. A short description of the stabilization can be found in Mehlmann and Korn (2021).

In Gascoigne the sea ice momentum equation is approximated with an implicit Euler method in time. The system is solved with a Newton scheme (Mehlmann & Richter, 2017b) and the resulting linear systems of equations are approximated with the GMRES method preconditioned by a parallel multigrid method (Failer & Richter, 2020; Mehlmann & Richter, 2017a). The nonlinear system is solved to a tolerance of  $10^{-13}$ , whereas the linear problems in each Newton step are computed with an accuracy of  $10^{-2}$ .

The tracers, which are placed on cell centers in the B-grid and CD-grid staggering, are advected with an upwind scheme. For A-grid-like discretization, the tracers are placed on vertices and a Flux-Corrected transport scheme is used (Mehlmann, 2019).

#### 4.1.2. MITgcm (C-Grid Placement on Quadrilaterals)

We apply the sea ice module of the MITgcm (Losch et al., 2010) for Arakawa C-grid simulations on quadrilateral grids. In the MITgcm, the momentum equations and in particular the divergence of the stress tensor

are discretized using a finite-volume method on a quadrilateral, curvilinear Arakawa C-grid. The strain rate tensor components, are approximated by central differences. Details of the discretization can be found in the appendix of Losch et al. (2010) or at <https://mitgcm.readthedocs.io>.

The momentum equations use an implicit Euler method in time. In each time step, the nonlinear system of equations is solved implicitly using a Jacobian-free Newton Krylov (JFNK) solver (Losch et al., 2014). An inexact Newton method is used, where the linear system is solved with an accuracy depending on the nonlinear convergence rate. The nonlinear solution required to have a residual  $10^{-4}$  times smaller than the initial residual. For details see Losch et al. (2014) or <https://mitgcm.readthedocs.io>. Ice thickness and concentration are advected with a second order scheme with a superbee flux limiter.

#### 4.1.3. CICE (B-Grid Placement on Quadrilaterals)

The sea ice model CICE (Hunke et al., 2015) is used for Arakawa B-grid simulations. On a sub grid level in the Arakawa B-grid setup of CICE, the sea ice velocity and the stresses are discretized using bilinear basis functions in a finite element sense (Hunke et al., 2015). In CICE, the VP solution is calculated using a recently implemented Picard solver. The nonlinear solution is approximated by performing 100 Picard iterations. The linear system is solved until the relative criterion  $10^{-2}$  is reached. Details on the solver choice and configurations are discussed in Section 6. The tracers in CICE are transported with the incremental remapping scheme (Lipscomb & Hunke, 2004).

By default, CICE uses an ice-thickness-distribution (ITD) model with five thickness categories. As the initial ice thickness is 0.3 m and the thickness does not exceed 0.46 m during our simulations, only the first category with an upper limit of 0.64 m is populated. Ice strength  $P_0$  in Equation 8 is computed from the sum over all thickness categories, so that our CICE simulations are equivalent to simulations with only one thickness category. Note that the strength parameterization is different from the CICE default.

#### 4.1.4. FESOM (A-Grid, B-Grid, CD-Grid on Triangles)

FESOM by default applies a P1-P1 finite element discretization, which is based on an A-grid placement of the variables (see Danilov et al., 2015, for details). For this study also a finite-volume B grid and a CR-P0 finite element pair, using a CD-grid placement of the variables, have been realized. The B-grid placement corresponds to the quasi-B grid staggering used in MPAS (Petersen et al., 2019). In analogy to the quadrilateral case, P1 and CR refer to the piecewise linear element and the nonconforming linear element on triangles. As on quadrilateral meshes, the space of finite elements that corresponds to a C-grid staggering is too small to approximate the strain rate tensor (Acosta et al., 2011). Instead, this issue motivates the use of the Arakawa CD-grid placement on triangular meshes. As outlined for the quadrilateral case (Section 4.1.1) we use a stabilized version of the CD-grid-like CR-P0 finite element. The quasi-B-grid discretization on triangular meshes may also suffer from noise in the velocity field if strain rates are computed at vertices or triangles. We stabilized the approximation by reconstructing the strain rates at the element-edges (Danilov et al., 2021).

In FESOM, the discretization of the sea ice momentum equation is based on the explicit mEVP solver. For a large number of sub-cycles per time step the method converges to the VP solution (Kimmritz et al., 2015). However, in practice only a limited number of iterations of the mEVP solver are applied to reduce the numerical cost (Koldunov et al., 2019). We follow the suggestion of Koldunov et al. (2019) and use 100 sub-cycle steps per time step, which has been shown to be a good compromise between the number of LKFs resolved and the numerical cost. We discuss the impact of the number of subiterations in Section 6. In the A-grid and B-grid discretization the tracers are advected with a flux-correction scheme (Löhner et al., 1987), whereas the CD-grid set up uses an upwind scheme.

#### 4.1.5. ICON (CD-Grid on Triangles)

The FESOM CD-grid implementation follows the implementation of the sea ice module in ICON (Mehlmann & Korn, 2021) and differs by using longitude-latitude coordinates, whereas coordinate systems local to triangles are used in ICON. Since the test case is done in plane geometry, both approaches are expected to lead to the same result. By default the ICON grid uses equilateral triangles. Thus, straight boundaries cannot be represented on all sides of the area considered in benchmark problem. Therefore the boundaries on the left (west) and right (east) hand side of the domain are formed by outward pointing triangles (Figure 7).

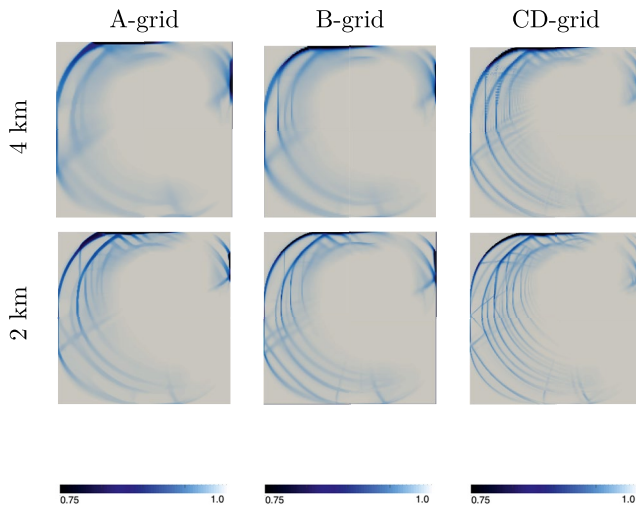


**Figure 3.** Sea ice concentration after 2 days of simulation (1,440 iterations) computed on a quadrilateral mesh in Gascoigne.

## 4.2. Choice of Grids

The benchmark problem is analyzed on quadrilateral and triangular meshes with grid spacings of 8, 4, and 2 km. The corresponding quadrilateral meshes have 4,096, 16,384, and 65,536 cells. To compare the two CD-grid type discretizations in FESOM and ICON we also use meshes with standard side lengths. In contrast to ICON, the boundaries are straight in FESOM with additional rectangular triangles along the west and the eastern boundaries. This implies that the boundary triangles are not equilateral. The triangular 8 km grid in ICON has 9,070 cells, the 4 km grid has 37,082 cells, and the 2 km mesh contains 149,938 cells, whereas the triangular mesh in FESOM consists of 9,490 cells (8 km), 37,926 cells (4 km), and 151,630 cells (2 km).

An appropriate measure to compare triangular and quadrilateral grids is the total number of vertices. This is so, because the geometric resolution (in the sense of resolvable wave numbers) of a particular mesh is defined by the unit cell, which is a translationally invariant element of the mesh. A unit cell of a triangular mesh is a rhombus formed by two triangles, and the number of unit cells is equivalent to the number of vertices. To compare the discretizations on quadrilateral and triangular meshes we

chose grids with the same number of vertices. Therefore the edge lengths in the triangular case are slightly larger with 8.6, 4.3, and 2.15 km. Keeping the same number of vertices in the triangular grid results in twice as many cells and 1.5 times more edges than on quadrilateral meshes.

We solve the system on all mesh levels with a time step of  $\Delta t = 2$  min. The choice of time step is determined by the use of the explicit mEVP solver on the 2 km grid. The discretization with a CD-grid-like placement requires slightly smaller time steps than the approximation based on the A-grid or the B-grid type staggering. The effect is discussed in Danilov et al. (2021)

## 5. Numerical Evaluation

In this section, we examine the effect of the grid staggering on the formation of LKFs. To quantify the effect, we analyze the sea ice concentration  $A$  and shear deformation (Equation 9).

### 5.1. Gascoigne (A-Grid, B-Grid, CD-Grid Staggering on Quadrilaterals)

We start by considering the discrete solutions obtained with different finite element discretizations available in Gascoigne (Becker et al., 2021). The B-grid and the CD-grid-like finite element discretization differ only by the staggering of the velocity components while the A-grid type and B-grid-like finite element discretizations are identical except for the placement of the sea ice concentration and thickness.

As both B-grid and CD-grid-like approximations are based on an upwind scheme, we can attribute the relatively large differences in the sea ice concentration in Figure 3 to the different velocity placement. Generally, the sea ice concentration obtained with CD-grid-like discretization has more details than the corresponding approximation with A- and B-grid-like staggering. This goes so far that the 4 km-solution with CD-grid staggering is qualitatively similar to the sea ice concentrations obtained with the 2 km A-grid and B-grid-like discretizations.

The results of the CD-grid staggering show a peculiarity: especially on coarse grids (8 km), many LKFs are identified (Figures 4 and 5). A closer analysis of the detected features shows that numerical artifacts along the boundary are incorrectly identified as features. These artifacts, which are also visible close to the boundaries in the shear deformation (Figure 6) on the 4 and 2 km meshes (although they are not identified as features here), as well as the pattern that is visible in upper left corner of the shear deformation and to some extent in the sea ice concentration are not numerical instabilities but originate from the approximation properties of the finite element space. They diminish with increasing resolution and can be explained

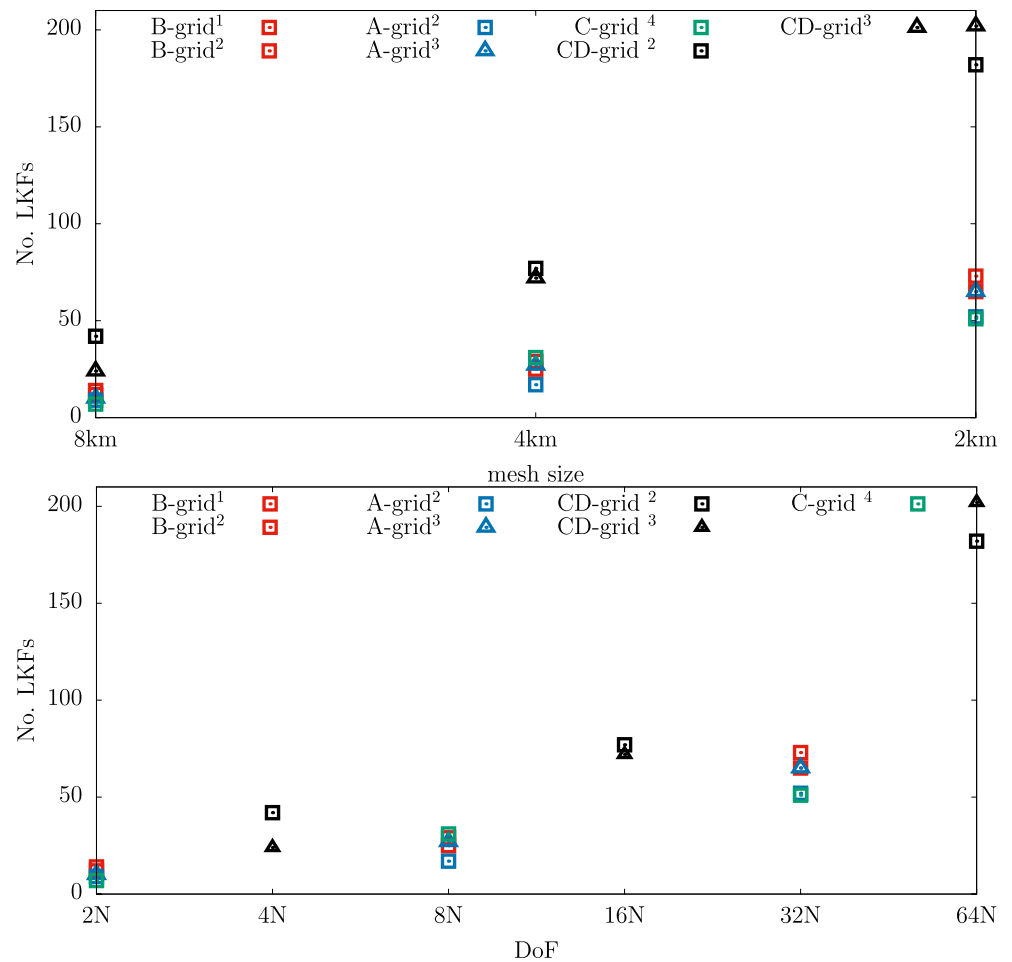


**Figure 4.** The number of the detected linear kinematic features from the shear deformation field presented in Figures 6 and 9 on quadrilateral □ and triangular △ meshes.  $N$  indicates the number of cells on the different meshes. The superscripts 1, 2, 3, and 4 refer to the simulations carried out in the framework of CICE, Gascoigne, FESOM, and MITgcm respectively.

as follows: In case of the quadrilateral CD-grid, the finite element space contains a nonlinear term  $x^2 - y^2$  in addition to the linear polynomials. This extra term does not improve the approximation quality and causes an oscillatory behavior within each element. Note the the CD-grid approximation on triangular grids does not have this property. As most of features are wider than a grid cell and persists under mesh refinement we do not attribute them as numerical noise but to the inability of the finite element space to resolve "straight lines." A possibility to smooth this pattern in the tracers might be the use of a advection scheme with less DoF such as first order Flux-Corrected transport.

In the case of the A-grid discretization, however, the sea ice concentration and sea ice thickness are advected with a second order Taylor-Galerkin flux-correction scheme (Mehlmann, 2019), so that the much smaller differences between A-grid and B-grid (Figure 3) have to be attributed to a combination of different tracer point placement and the related difference in advection schemes. This indicates that neither the advection scheme nor the placement of the tracers are important for the evolution of LKFs in this test case.

## 5.2. MITgcm (C-Grid Placement on Quadrilaterals) and CICE (B-Grid Placement on Quadrilaterals)

The MITgcm configuration differs from Gascoigne's B-grid and CD-grid type setups by the placement and discretization of the sea ice velocity and the choice of advection scheme (second order finite volume scheme

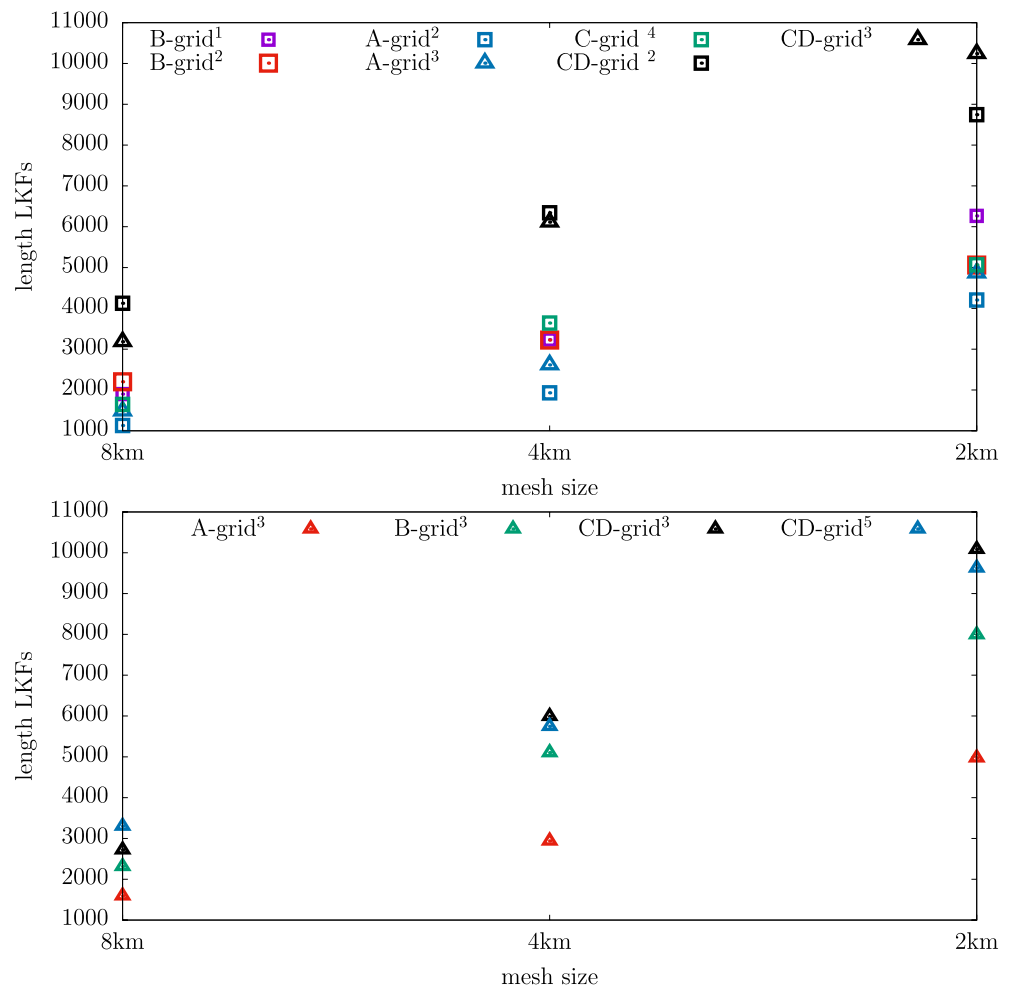


**Figure 5.** The length of the detected linear kinematic features on quadrilateral (left) triangular meshes (right). The superscripts 1, 2, 3, 4, and 5 refer to the simulations carried out in the framework of CICE, Gascoigne, FESOM, MITgcm, and ICON, respectively.

with a superbee flux limiter). The C-grid type discretization resolves less structure in the sea ice concentration and shear deformation than the CD-grid-like finite element discretization in Gascoigne (Figure 6). The same is true for the detected number and total length of LKFs (Figures 4 and 5).

CICE uses a B-grid type staggering such as the Q1-Q0 finite element discretization in Gascoigne. The sea ice thickness and concentration are advected with the incremental remapping scheme (Lipscomb & Hunke, 2004). Figure 6 shows that the LKFs in the CICE discretization are wider than the LKFs in the B-grid-like Gascoigne approximation. Furthermore, the simulated sea ice concentration is more diffusive. We observe that the CICE simulation produces fewer LKFs in the sea ice concentration and shear deformation field (Figure 6) than the approximation based on a CD-grid placement, see Figures 4 and 5.

### 5.3. FESOM (A-Grid, B-Grid, CD-Grid Placement on Triangles)

We now consider the A-grid-like and B-grid type discretization in FESOM. Figure 7 shows in the first and second column the sea ice concentration and shear deformation approximated with an A-grid and B-grid type staggering in FESOM. As the only difference between the two approximations is the staggering and discretization of the velocity field, we attribute the difference shown in sea ice concentration and shear deformation (Figure 7) to the discretization of the sea ice velocity. Figure 7 shows that the CD-grid approximation

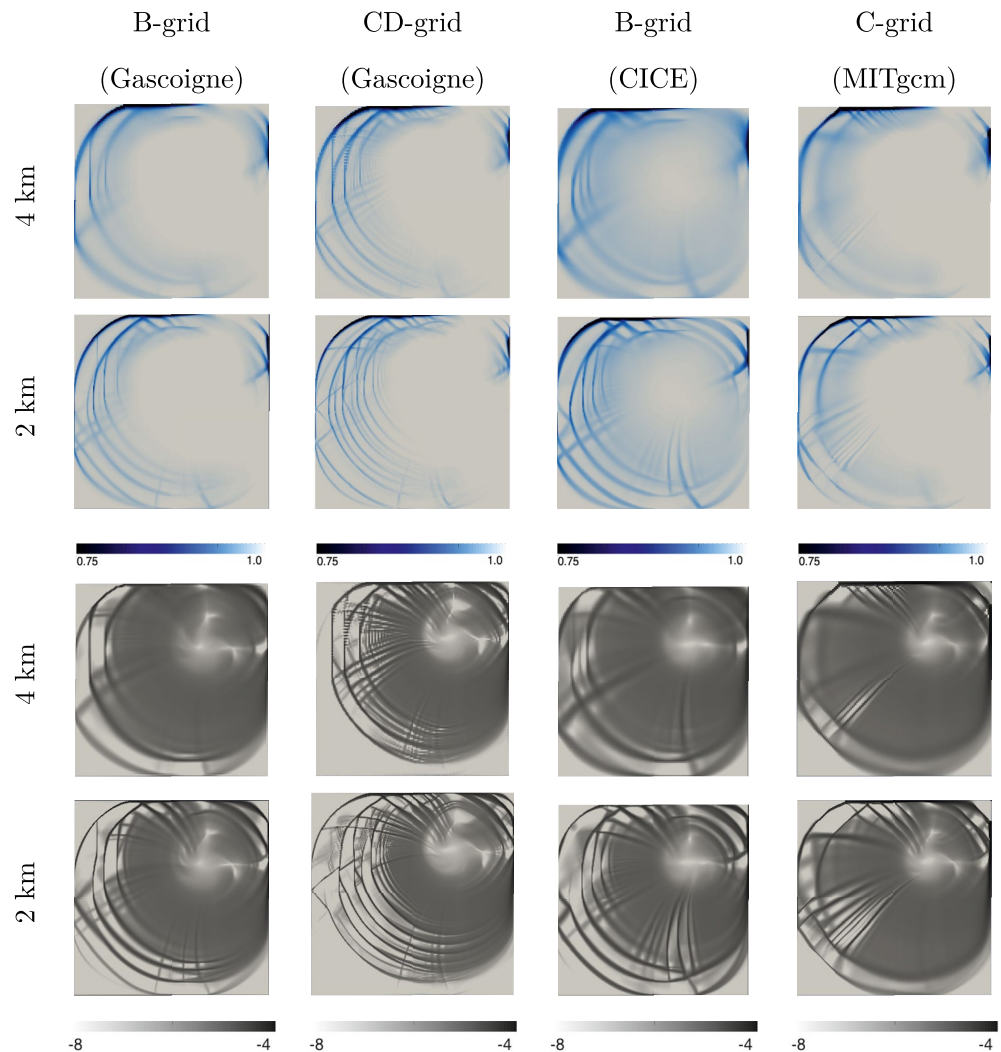


**Figure 6.** The first and second row show the sea ice concentration. The third and fourth row present the shear deformation calculated on a quadrilateral mesh. The snapshots are taken after 2 days of simulation. The shear deformation is given in  $s^{-1}$  and plotted in logarithmic scale.

in FESOM produces more LKFs than the A-grid and B-grid-like discretization on the same mesh. The same is observed for the detected number and total length of LKFs (Figures 5 and 8).

#### 5.4. ICON (CD-Grid Staggering on Triangles)

The reader is reminded that the approximation in ICON is based on equilateral triangles, whereas FESOM adds rectangular triangles to represent the smooth boundaries (Section 4.2). Otherwise, both CD-grid-like discretizations are the same.

The sea ice concentration and the shear deformation presented in Figure 7 are similar in both cases. We conclude that the castellated western and eastern boundaries in ICON have a small impact on the number of resolved LKFs. This finding is supported by the results of the LKFs detection algorithm shown in Figures 5 and 8. Both CD-grid-like discretizations resolve a similar number and total length of LKFs on the 8, 4, and 2 km meshes.

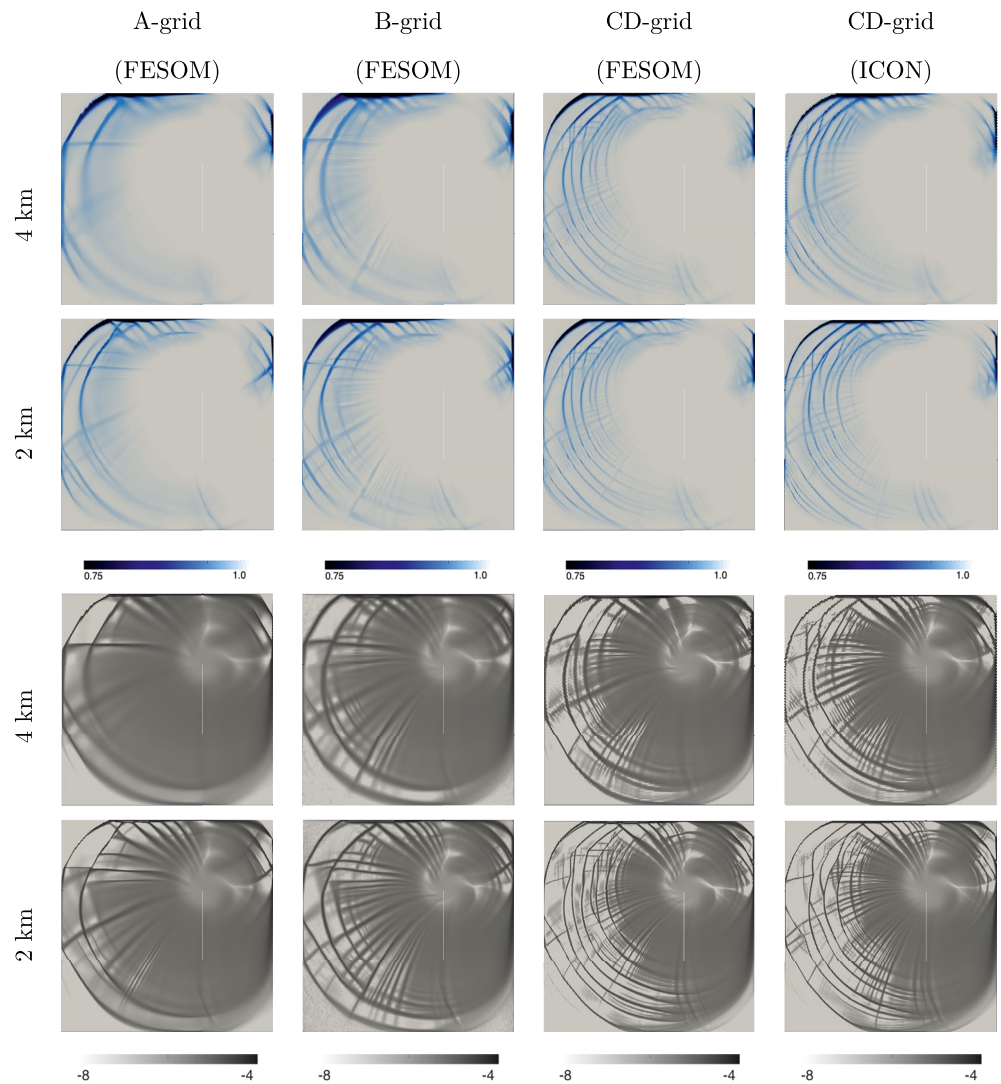


**Figure 7.** The first and second row show the sea ice concentration. The third and fourth row present the shear deformation calculated on a triangular mesh. The snapshots are taken after 2 days of simulation. The shear deformation is given in  $s^{-1}$  and plotted in logarithmic scale.

### 5.5. Comparison of Quadrilateral and Triangular Grids

In this section, we compare the approximation of sea ice dynamics on quadrilateral and triangular grids with respect to their ability to resolve LKFs. The triangular grids contain twice as many cells as the quadrilateral grids, but the same number of vertices. The discretization on the triangular grids is done in the framework of the sea ice model FESOM using an A-grid type and CD-grid type staggering.

Figure 9 compares the approximations of the sea ice concentration with A-grid and CD-grid type discretizations on quadrilateral grids to those on triangular grids. We observe that the A-grid solution using triangles is qualitatively similar to the A-grid solution with quadrilaterals. The same conclusion is drawn for the CD-grid staggering. We conclude that, given the same number of vertices, the formation of LKFs is more sensitive to the velocity staggering than to the use of quadrilateral or triangular grids. This is supported by the results of the detection algorithm (Figures 4 and 5). The number and total length of LKFs is similar for the CD-type discretization on the structured quadrilateral and triangular meshes. The same is true for the A-grid type discretizations. Figure 4 also shows that the Arakawa B-grid and C-grid discretizations on structured quadrilateral meshes resolve quantitatively the same number of LKFs as an A-grid-like approximation on triangular meshes.

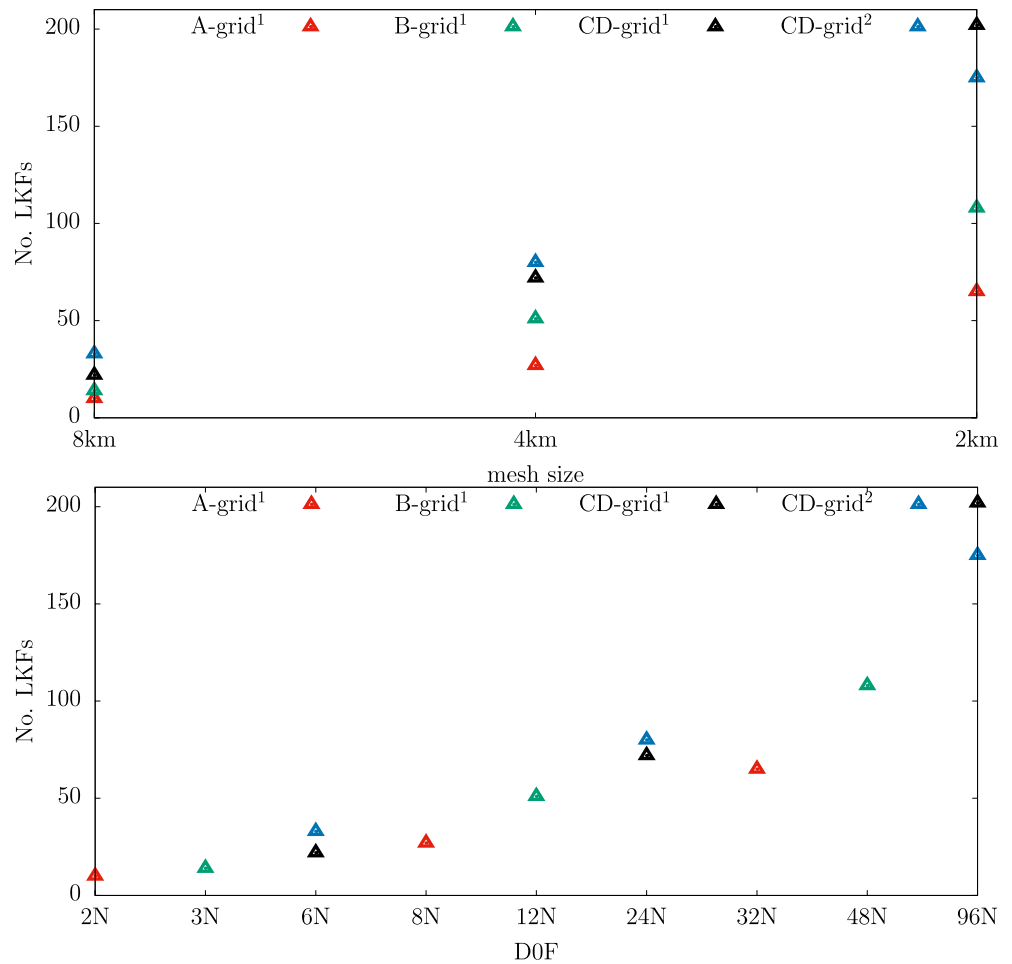


**Figure 8.** The number of the detected LKFs on triangular meshes from the shear deformation presented in Figure 7.  $N$  is the number of cells. The superscripts 1 and 2 refer to the simulation carried out in the sea ice module of FESOM and ICON respectively.

## 6. Discussion

We found that the LKF detection algorithm introduces some uncertainty into our analysis. The algorithm tends to split features at intersection, so that in some cases one additional LKF that intersects a second one can lead to a count of four. For this reason, the algorithm tends to overestimate the number of LKFs for the approximations with CD-grid-like staggering, where small and short scale features appear more often compared to the other grid staggerings. For this reason, the total length of all detected features appears to be a more robust metric. Therefore, we will discuss only those properties of the discretizations that show a clear tendency in all three measures, the number of LKFs, the length of LKFs and the direct visual evaluation of the approximation.

The numerical results presented in Section 5 show that among the different model discretizations, approximations with a CD-grid staggering resolved the most LKFs. One reason is the fact that the CD-type discretization has more velocity degrees of freedom (DoFs). As a consequence, sharper gradients are resolved and a better approximation of the strain rate tensor is obtained. Furthermore, the comparison of the quadrilateral A-grid, B-grid and CD-grid like discretizations in Gascoigne (Figure 3) indicates that the approximation of the strain rate tensor is the most important term of the stress tensor.

On quadrilateral meshes, the CD-grid-like approximation has twice as many DoFs as the A-grid, B-grid or C-grid type staggering. As a consequence, if a 4 km mesh has  $N$  grid cells and  $2N$  velocity DoFs for an A-, B-, or C-grid (2 per grid cell), the CD-grid has  $4N$  DoFs. However, the CD-grid setups resolve at least twice

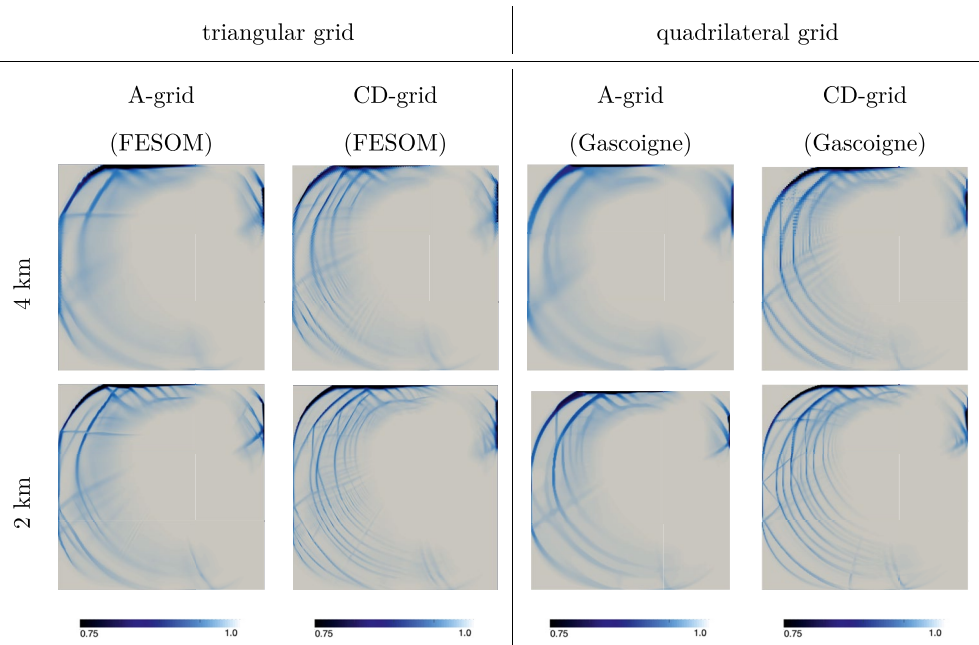


**Figure 9.** Sea ice concentration on triangular and quadrilateral meshes using the same number of vertices. Therefore the edge length in the triangular case is 8.6, 4.3, and 2.15 km. The triangular mesh has around double the number of cells and 1.5 more edges compared to the quadrilateral mesh. The snapshots are taken after two days of simulation (1,440 iterations).

as many LKFs (Figure 4), so that simulations on a 4 km CD-grid ( $4N$  DoFs) appear very similar to simulations with A, B, and C-grid staggering on 2 km meshes with  $8N$  DoFs (Figure 4, upper panel and Figure 5, left panel). On triangular meshes, the CD-grid-like discretization resolves almost the same number and total length of LKFs on the 4 km grid ( $6N$  DoFs) as the A-grid type discretization on the 2 km mesh ( $8N$  DoFs) (Figures 4 and 5). So, even on meshes with fewer DoFs, a similar amount of LKFs are detected with the CD-grid approximation. However, fewer LKFs are detected in the triangular CD-grid-like discretization on meshes with a lower number of DoF ( $6N$ ) than the triangular B-grid-like approximation ( $12N$ ) (Figure 8).

Previous work suggests that a more accurate solution leads to more and better defined LKFs (Koldunov et al., 2019; Lemieux & Tremblay, 2009; Lemieux et al., 2012). Results for our benchmark problem indicate that the approximate solutions are sufficiently converged as the number of LKFs does not significantly grow if the number of subiterations in the mEVP solver or in the Picard is increased (not shown). Similarly, a higher solver tolerance for the Newton methods does not influence the number of resolved LKFs.

The implicit solvers are much more robust to numerical details than the mEVP solver. For example, the mEVP solver requires careful tuning of the stabilization parameters ( $\alpha, \beta$  Kimmritz et al., 2015) for each new grid (Danilov et al., 2021; Kimmritz et al., 2015). In addition, the stabilization of the CD-grid-like staggering requires a weight that is independent of the spatial resolution. While the choice of this weight is described in Mehlmann and Korn (2021) in the context of implicit solvers, its value needs to be tuned for the mEVP solver (Danilov et al., 2021). The optimal configuration for the mEVP solver remains an open question.

We repeated the experiment with the MITgcm sea ice module with extreme choices of advection schemes, a first-order upwind scheme and a seventh-order monotonicity preserving advection scheme and conclude that the advection scheme is not important in our context (results not shown). The result is supported by similar experiments with CICE and FESOM using an upwind advection scheme. Finally, we point out that our analysis does not allow any conclusions about the differences in simulated LKFs between finite element, finite volume and finite difference discretizations. We assume that these differences are small as the deformation fields simulated by CICE (B-grid, finite difference) and Gascoigne (B-grid, finite element)

are similar, see Figure 6. But there are too many confounders such as different advection schemes to draw reliable conclusions.

## 7. Conclusion

To conclude, we found in a comparison of different viscous-plastic sea ice models that the staggering and discretization of the velocity vector components on a grid with a given spatial resolution can have a large effect on the formation of linear kinematic features (LKFs). Approximations with a CD-grid staggering lead to more LKFs than the commonly used A, B, and C-grid discretizations. A, B, and C-grid discretization resolved similar amounts of LKFs.

Besides the discretization of the velocities, other factors such as the geometry of the cell (triangular or quadrilateral), the staggering of the tracers, the advection scheme for the tracers, and the time step are less important for the production of LKFs in our specific test case. These factors mainly affect width and definition of the LKFs and their position in the domain. We expect that details such as the advection scheme would become more important in longer simulations with larger ice displacements.

On quadrilateral meshes, the CD-grid discretization doubles the degrees of freedom per grid cell for the velocity field and triples them on triangular meshes compared to an A-grid-like discretization. Even so, we found that the CD-grid-like approximation produces more LKFs on meshes with fewer DoFs compared to A, B, C-grid type discretizations on quadrilateral and A-grid-like discretization on triangular meshes. Furthermore, a CD-grid discretization allows us to resolve more LKFs on grids that have a grid spacing that is a factor of two larger than with conventional grid staggering. This is an appealing property because simulating realistic LKFs in the viscous-plastic sea ice model requires high spatial resolution.

## Data Availability Statement

The data and the routines to process it are available in a Mendeley data repository (Mehlmann et al., 2021).

## References

- Acosta, G., Apel, T., Duran, R., & Lombardi, A. (2011). Error estimates for Raviart-Thomas interpolation of any order on anisotropic tetrahedra. *Mathematics of Computation*, 80, 141–163. <https://doi.org/10.1090/S0025-5718-2010-02406-8>
- Becker, R., Braack, M., Meidner, D., Richter, T., & Vexler, B. (2021). *The finite element toolkit Gascoigne 3D [Computer software manual]*. Retrieved from <https://www.gascoigne.de>
- Blockley, E., Vancoppenolle, M., Hunke, E. C., Bitz, C., Feltham, D. L., Lemieux, J.-F., et al. (2020). The future of sea ice modeling: Where do we go from here? *Bulletin of the American Meteorological Society*, 101(8), 1304–1311. <https://doi.org/10.1175/bams-d-20-0073.1>
- Bouchat, A., & Tremblay, B. (2017). Using sea-ice deformation fields to constrain the mechanical strength parameters of geophysical sea ice. *Journal of Geophysical Research: Oceans*, 122(7), 5802–5825. <https://doi.org/10.1002/2017JC013020>
- Bouillon, S., Fichefet, T., Legat, V., & Madec, G. (2013). The elastic-viscous-plastic method revisited. *Ocean Modelling*, 71, 2–12. <https://doi.org/10.1016/j.ocemod.2013.05.013>
- Braess, D. (2007). *Finite elements: Theory, fast solvers, and applications in solid mechanics* (3rd ed.). Cambridge University Press. <https://doi.org/10.1017/CBO9780511618635>
- Coon, M., Kwok, R., Levy, G., Pruis, M., Schreyer, H., & Sulsky, D. (2007). Arctic Ice Dynamics Joint Experiment (AIDJEX) assumptions revisited and found inadequate. *Journal of Geophysical Research: Oceans*, 112(C11). <https://doi.org/10.1029/2005JC003393>
- Crouzeix, M., & Raviart, P.-A. (1973). Conforming and nonconforming finite element methods for solving the stationary Stokes equations I. *ESAIM: Mathematical Modelling and Numerical Analysis-Modélisation Mathématique et Analyse Numérique*, 7, 33–75. <https://doi.org/10.1051/m2an/197307r300331>
- Danilov, S., Mehlmann, C., & Fofonova, V. (2021). *On discretizing sea-ice dynamics on triangular meshes using vertex, cell or edge velocities*. arXiv:2106.13641.
- Danilov, S., Wang, Q., Timmermann, R., Iakovlev, N., Sidorenko, D., Kimmritz, M., et al. (2015). Finite-Element Sea Ice Model (FESIM), version 2. *Geoscientific Model Development*, 8, 1747–1761. <https://doi.org/10.5194/gmd-8-1747-2015>
- Dansereau, V., Weiss, J., Saramito, P., & Lattes, P. (2016). A Maxwell elasto-brittle rheology for sea ice modelling. *The Cryosphere*, 10(3), 1339–1359. <https://doi.org/10.5194/tc-10-1339-2016>
- Failor, L., & Richter, T. (2020). A parallel Newton multigrid framework for monolithic fluid-structure interactions. *Journal of Scientific Computing*, 82(2). <https://doi.org/10.1007/s10915-019-01113-y>
- Feltham, D. L. (2008). Sea ice rheology. *Annual Review of Fluid Mechanics*, 40(1), 91–112. <https://doi.org/10.1146/annurev.fluid.40.111406.102151>
- Gao, G., Chen, C., Qi, J., & Beardsley, R. C. (2011). An unstructured-grid, finite-volume sea ice model: Development, validation, and application. *Journal of Geophysical Research: Oceans*, 116(C8). <https://doi.org/10.1029/2010JC006688>
- Girard, L., Bouillon, S., Weiss, J., Amtrano, D., Fichefet, T., Thierry, L., & Legat, V. (2011). A new modeling framework for sea-ice mechanics based on elasto-brittle rheology. *Annals of Glaciology*, 52, 123–132. <https://doi.org/10.3189/172756411795931499>

## Acknowledgments

The authors thank Bruno Tremblay and the two anonymous reviewers for their valuable comments on our manuscript. Open access funding enabled and organized by Projekt DEAL.

- Gray, J. M. N. T., & Morland, L. W. (1994). A two-dimensional model for the dynamics of sea ice. *Philosophical Transactions of the Royal Society of London. Series A: Physical and Engineering Sciences*, 347(1682), 219–290.
- Hibler, W. D. (1979). A dynamic thermodynamic sea ice model. *Journal of Physical Oceanography*, 9, 815–846. [https://doi.org/10.1175/1520-0485\(1979\)009<0815:adtsim>2.0.co;2](https://doi.org/10.1175/1520-0485(1979)009<0815:adtsim>2.0.co;2)
- Hunke, E. C. (2001). Viscous-plastic sea ice dynamics with the EVP model: Linearization issues. *Journal of Computational Physics*, 170, 18–38. <https://doi.org/10.1006/jcph.2001.6710>
- Hunke, E. C., & Dukowicz, J. K. (1997). An elastic-viscous-plastic model for sea ice dynamics. *Journal of Physical Oceanography*, 27, 1849–1867. [https://doi.org/10.1175/1520-0485\(1997\)027<1849:aevpmf>2.0.co;2](https://doi.org/10.1175/1520-0485(1997)027<1849:aevpmf>2.0.co;2)
- Hunke, E. C., Lipscomb, W., Turner, A., Jeffery, N., & Elliott, S. (2015). *CICE: The Los Alamos sea ice model documentation and software user's manual version 5.1 LA-CC-06-012 [Computer software manual]*. Los Alamos National Laboratory.
- Hutchings, J., Heil, P., & Hibler, W. (2005). Modeling linear kinematic features in sea ice. *Monthly Weather Review*, 133, 3481–3497. <https://doi.org/10.1175/mwr3045.1>
- Hutter, N., & Losch, M. (2020). Feature-based comparison of sea ice deformation in lead-permitting sea ice simulations. *The Cryosphere*, 14(1), 93–113. <https://doi.org/10.5194/tc-14-93-2020>
- Hutter, N., Losch, M., & Menemenlis, D. (2018). Scaling properties of Arctic sea ice deformation in a high-resolution viscous-plastic sea ice model and in satellite observations. *Journal of Geophysical Research: Oceans*, 170, 18–38. <https://doi.org/10.1002/2017jc013119>
- Hutter, N., Zampieri, L., & Losch, M. (2019). Leads and ridges in Arctic sea ice from RGPS data and a new tracking algorithm. *The Cryosphere*, 13(2), 627–645. <https://doi.org/10.5194/tc-13-627-2019>
- Ip, C. F., Hibler, W. D., & Flato, G. M. (1991). On the effect of rheology on seasonal sea-ice simulations. *Annals of Glaciology*, 15, 17–25. <https://doi.org/10.1017/s0260305500009496>
- Kimritz, M., Danilov, S., & Losch, M. (2015). On the convergence of the modified elastic-viscous-plastic method for solving the sea ice momentum equation. *Journal of Computational Physics*, 296, 90–100. <https://doi.org/10.1016/j.jcp.2015.04.051>
- Koldunov, N., Danilov, S., Sidorenko, D., Hutter, N., Losch, M., Goessling, H., et al. (2019). Fast EVP solutions in a high-resolution sea ice model. *Journal of Advances in Modeling Earth Systems*, 11(5), 1269–1284. <https://doi.org/10.1029/2018ms001485>
- Kwok, R., Hunke, E. C., Maslowski, D., & Zhang, J. (2008). Variability of sea ice simulations assessed with RGPS kinematics. *Journal of Geophysical Research: Oceans*, 113(C11). <https://doi.org/10.1029/2008jc004783>
- Lemieux, J.-F., Knoll, D., Losch, M., & Girard, C. (2014). A second-order accurate in time IMplicit-EXplicit (IMEX) integration scheme for sea ice dynamics. *Journal of Computational Physics*, 263, 375–392. <https://doi.org/10.1016/j.jcp.2014.01.010>
- Lemieux, J.-F., Knoll, D., Tremblay, B., Holland, D., & Losch, M. (2012). A comparison of the Jacobian-free Newton-Krylov method and the EVP model for solving the sea ice momentum equation with a viscous-plastic formulation: A serial algorithm study. *Journal of Computational Physics*, 231, 5926–5944. <https://doi.org/10.1016/j.jcp.2012.05.024>
- Lemieux, J.-F., & Tremblay, B. (2009). Numerical convergence of viscous-plastic sea ice models. *Journal of Geophysical Research: Oceans*, 114(C5). <https://doi.org/10.1029/2008jc005017>
- Lemieux, J.-F., Tremblay, B., Sedláček, J., Tupper, P., Thomas, S., Huard, D., & Auclair, J. (2010). Improving the numerical convergence of viscous-plastic sea ice models with the Jacobian-free Newton-Krylov method. *Journal of Computational Physics*, 229, 2840–2852. <https://doi.org/10.1016/j.jcp.2009.12.011>
- Lipscomb, W. H., & Hunke, E. C. (2004). Modeling sea ice transport using incremental remapping. *Monthly Weather Review*, 132(6), 1341–1354. [https://doi.org/10.1175/1520-0493\(2004\)132<1341:msitui>2.0.co;2](https://doi.org/10.1175/1520-0493(2004)132<1341:msitui>2.0.co;2)
- Löhner, R., Morgan, K., Peraire, J., & Vahdati, M. (1987). Finite-element flux-corrected transport (FEM-FCT) for the Euler and Navier-Stokes equations. *International Journal for Numerical Methods in Fluids*, 7, 1093–1109. <https://doi.org/10.1002/flid.1650071007>
- Losch, M., Fuchs, A., Lemieux, J.-F., & Vanselow, A. (2014). A parallel Jacobian-free Newton-Krylov solver for a coupled sea ice-ocean model. *Journal of Computational Physics*, 257, 901–911. <https://doi.org/10.1016/j.jcp.2013.09.026>
- Losch, M., Menemenlis, D., Campin, J.-M., Heimbach, P., & Hill, C. (2010). On the formulation of sea-ice models. Part 1: Effects of different solver implementations and parameterizations. *Ocean Modelling*, 33(1), 129–144. <https://doi.org/10.1016/j.ocemod.2009.12.008>
- Mehlmann, C. (2019). *Efficient numerical methods to solve the viscous-plastic sea ice model at high spatial resolutions* (Doctoral dissertation). Otto-von-Guericke-Universität Magdeburg, Fakultät für Mathematik. <https://doi.org/10.25673/14011>
- Mehlmann, C., Danilov, S., Losch, M., Lemieux, J.-F., Hutter, N., Richter, T., et al. (2021). *Sea ice numerical VP-comparison benchmark*. Mendeley Data. <https://doi.org/10.17632/kj58y3sdtk.1>
- Mehlmann, C., & Korn, P. (2021). Sea-ice dynamics on triangular grids. *Journal of Computational Physics*, 428, 110086. <https://doi.org/10.1016/j.jcp.2020.110086>
- Mehlmann, C., & Richter, T. (2017a). A finite element multigrid-framework to solve the sea ice momentum equation. *Journal of Computational Physics*, 348, 847–861. <https://doi.org/10.1016/j.jcp.2017.08.004>
- Mehlmann, C., & Richter, T. (2017b). A modified global Newton solver for viscous-plastic sea ice models. *Ocean Modelling*, 116, 96–107. <https://doi.org/10.1016/j.ocemod.2017.06.001>
- Petersen, M., Asay-Davis, X., Berres, A., Chen, Q., Feige, N., Hoffman, M., et al. (2019). An evaluation of the ocean and sea ice climate of E3SM using MPAS and interannual CORE-II forcing. *Journal of Advances in Modeling Earth Systems*, 11(5), 1438–1458. <https://doi.org/10.1029/2018ms001373>
- Rampal, P., Bouillon, S., Olason, E., & Morlighem, M. (2016). neXtSIM: A new Lagrangian sea ice model. *The Cryosphere*, 10, 1055–1073. <https://doi.org/10.5194/tc-10-1055-2016>
- Rannacher, R., & Turek, T. (1992). Simple nonconforming quadrilateral Stokes element. *Numerical Methods for Partial Differential Equations*, 8, 97–111. <https://doi.org/10.1002/num.1690080202>
- Richter, T. (2017). *Fluid-structure interactions*. Springer International Publishing.
- Stern, H. L., & Lindsay, R. W. (2009). Spatial scaling of Arctic sea ice deformation. *Journal of Geophysical Research: Oceans*, 114(C10), C10017. <https://doi.org/10.1029/2009JC005380>
- Tsamados, M. L., Feltham, D. L., & Wilchinsky, A. V. (2013). Impact of a new anisotropic rheology on simulations of Arctic sea ice. *Journal of Geophysical Research: Oceans*, 118(1), 91–107. <https://doi.org/10.1029/2012jc007990>
- Wang, K., & Wang, C. (2009). Modeling linear kinematic features in pack ice. *Journal of Geophysical Research: Oceans*, 114(C12). <https://doi.org/10.1029/2008JC005217>
- Zhang, J. L., & Hibler, W. D. (1991). On an efficient numerical method for modeling sea ice dynamics. *Journal of Geophysical Research: Oceans*, 102, 8691–8702.